MATERIALS CHEMISTRY FRONTIERS

RESEARCH ARTICLE

View Article Online
View Journal | View Issue

Cite this: *Mater. Chem. Front.*, 2025, **9**, 3469

Post-synthetic engineering of covalent organic frameworks with thiophene and naphthalimide units for enhanced oxygen reduction electrocatalysis

Elena Gala, [ab] Emiliano Martínez-Periñán, [*cd] Marcos Martínez-Fernández, [a] Marta Gordo-Lozano, [a] José I. Martínez [e] and José L. Segura [*a]

Received 3rd September 2025,
Accepted 28th October 2025

DOI: 10.1039/d5qm00655d

rsc.li/frontiers-materials

The development of efficient metal-free electrocatalysts for the oxygen reduction reaction (ORR) is essential for advancing sustainable energy technologies. In this work, we report the post-synthetic functionalization of covalent organic frameworks (COFs) with donor–acceptor (D–A) motifs incorporating thiophene and naphthalimide derivatives, yielding two novel materials. These COFs were synthesized *via* CuAAC click chemistry and thoroughly characterized. Electrochemical analyses revealed enhanced ORR activity in both materials, with one COF exhibiting near-ideal four-electron selectivity and remarkable stability. Density functional theory (DFT) calculations corroborated the experimental results, demonstrating that the electronic structure of COFs facilitates efficient O–O bond cleavage and electron transfer. These findings underscore the potential of rationally designed D–A COFs as high-performance, metal-free ORR electrocatalysts, contributing to the development of next-generation sustainable energy conversion technologies.

Introduction

Molecular oxygen (O_2) is one of the most abundant components of breathable air, and despite its high-bond-energy (498 kJ mol^{-1}), the cleavage of the O=O bond is essential for aerobic respiration.[1,2] Thus, the oxygen reduction reaction (ORR) is an inspiring counter reaction for sustainable energy conversion technologies (*e.g.*, hydrogen fuel cells and metal–air batteries).[3,4] However, this process shows two main drawbacks: (i) its slow kinetics and (ii) the H_2O_2/H_2O selectivity of the process, which is related to the energy conversion efficiency.[4–6] Both problems can be solved using suitable catalysts, enhancing the reaction rates and controlling the selectivity. However, the most widely used catalysts in energy conversion are platinum-based catalysts due to the high-performances offered by this noble metal. Nevertheless, the scarcity and high cost of platinum hinder their commercial viability and, consequently, recent research has focused on alternative electrocatalysts.[2,7]

In this field, metal-free electrocatalysts (MFEs) are gaining increasing attention due to their enhanced environmental compatibility.[8] These materials typically consist of polarized sp^2 carbon—light heteroatom bonds embedded within a conductive carbon matrix, generating active sites for the ORR.[9,10] Conventional MFE synthesis strategies include: (i) heteroatom doping of carbon materials, often resulting in heterogeneous distributions,[10] and (ii) pyrolysis of organic precursors.[11] However, these methods often compromise key catalyst properties such as porosity and atomic order, and the formation of active sites during doping or pyrolysis remains difficult to control.[8]

To address these limitations, covalent organic frameworks (COFs) have emerged as an ideal platform for the design of MFEs. In this sense, COFs combine intrinsic crystallinity, high surface areas (up to 4000 m^2 g^{-1}), and tunable architectures, making them excellent model systems for studying catalytic conversions.[1] Among the various active sites motifs investigated for ORR electrocatalysis —including thiophene derivatives or naphthalenediimides[12,13] —donor–acceptor (D–A) active sites remain largely underexplored, despite their potential to enhance catalytic performance through electronic charge redistribution (*e.g.*, Tafel slope reduction).[14,15]

[a] *Departamento de Química Orgánica I, Facultad de Ciencias Químicas, Universidad Complutense de Madrid, 28040, Madrid, Spain. E-mail: segura@ucm.es*
[b] *Departamento de Tecnología Química y Ambiental, Escuela Superior de Ciencias Experimentales y Tecnología, Universidad Rey Juan Carlos, 28933, Móstoles (Madrid), Spain*
[c] *Departamento de Química Analítica y Análisis Instrumental, Facultad de Ciencias, Universidad Autónoma de Madrid, 28049, Madrid, Spain. E-mail: emiliano.martinez@uam.es*
[d] *Institute for Advanced Research in Chemical Sciences (IAdChem), Universidad Autónoma de Madrid, 28049, Madrid, Spain*
[e] *Departamento de Nanoestructuras, Superficies, Recubrimientos y Astrofísica Molecular, Instituto de Ciencias de Materiales de Madrid (ICMM-CSIC), 28049, Madrid, Spain*

Herein, we report the post-synthetic modification of an "innocent" COF with various D–A motifs incorporating thiophene and naphthalenediimide-based active sites. In particular, we evaluated two new donor units: (i) unsubstituted thiophenes, which represent a benchmark in the design of state-of-the-art MFEs for ORR, and (ii) novel thienopyrrole derivatives, which are emerging as promising building blocks in fields such as solar-cells[16] and field effect transistors.[17] The resulting frameworks were characterized by solid-state techniques, confirming the successful integration of the new active sites within the porous network. Notably, incorporation of the D–A system led to enhanced electrocatalytic kinetics compared to the previously reported pure acceptor-based COF.[13]

Results and discussion

Synthesis and characterization of NDI-3T-COF and NDI-2TP-COF

The incorporation of ambipolar naphthalimide fragments into the COF pores required the preliminary synthesis of azide-functionalized building blocks. Accordingly, the preparation of the compound **N3-NIA** (Scheme 1) represented a key step toward obtaining the desired materials. To the best of our knowledge, no prior examples of naphthalenemonoimide derivatives bearing an azido group on the alkyl chain have been reported. Based on the method described by Dan Pantos and co-workers,[18] **N_3-NIA** was synthesized *via* microwave-assisted reaction between naphthalenetetracarboxylic dianhydride (**NTDA**) and 8-azidooctan-1-amine (**1**) in DMF (Scheme 1). Under these conditions, the naphthalimide derivative **N_3-NIA** was obtained as the sole detectable product in excellent yield (85%).

Following the synthesis of **N_3-NIA**, we proceeded with the preparation of the conjugated donor–acceptor molecules **N3-NDI-3T** and **N3-NDI-2TP** (Scheme 2). **N3-NDI-3T** was obtained *via* condensation of **N_3-NIA** with the diaminoterthiophene derivative **2** under the same conditions previously reported.[17] In contrast, the synthesis of **N3-NDI-2TP** proved more challenging due to the instability of diamine **2**, which was generated *in situ* by reduction of the benzothiadiazole derivative **BTD-2TP** using zinc powder in acetic acid (Scheme 2). Upon completion of the reduction, the resulting solution of compound **2** was transferred to a solution of **N_3-NIA** in acetic acid *via* cannula filtration.[17] This approach was adopted to prevent the introduction of residual zinc, which could potentially reduce the azido groups present in both **N_3-NIA** and the final product, **N3-NDI-2TP**. Characterization of both compounds by NMR, FTIR, and mass spectrometry confirmed that the azido functionality remained intact throughout the condensation processes (see SI).

The incorporation of donor–acceptor molecules **N3-NDI-3T** and **N3-NDI-2TP** into the pores of **[HC≡C]0.17-TPB-DMTP-COF** *via* copper(I)-catalyzed azide–alkyne cycloaddition (CuAAC) reaction click chemistry was successfully achieved (Scheme 2). The covalent attachment of these units was initially confirmed by solid-state cross-polarization magic angle spinning carbon-13 nuclear magnetic resonance (^{13}C-CP/MAS-NMR) spectroscopy. As shown in Fig. 1, the most significant changes are observed in the aliphatic region of the spectrum. Notably, the disappearance of signals corresponding to sp-hybridized carbon (70–80 ppm) and the appearance of a strong signal at ~30 ppm, attributed to the methylene groups of the ambipolar fragments, confirm the successful modification. In the aromatic region, the broadening of the signal around 130 ppm is consistent with the presence of **NDI-3T** and **NDI-2TP** moieties (Fig. S6 and S8). Additional spectroscopic characterization was carried out using UV-Vis and FTIR spectroscopy (Fig. S16–S18). In the FTIR spectra, the disappearance of the characteristic azide stretching band at 2100 cm^{-1}, along with the retention of the carbonyl stretching bands from the NDI units, confirmed complete coupling and the absence of residual **N3-NDI-3T** or **N3-NDI-2TP**. The disappearance of both azide and alkyne vibrational features in the FTIR spectra, together with the

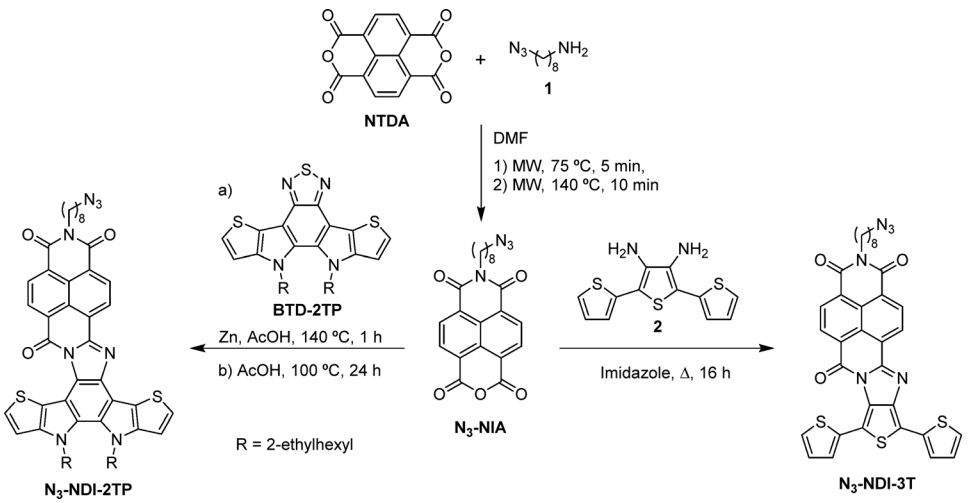

Scheme 1 Synthesis of **N_3-NIA**, **N3-NDI-3T** and **N3-NDI-2TP**.

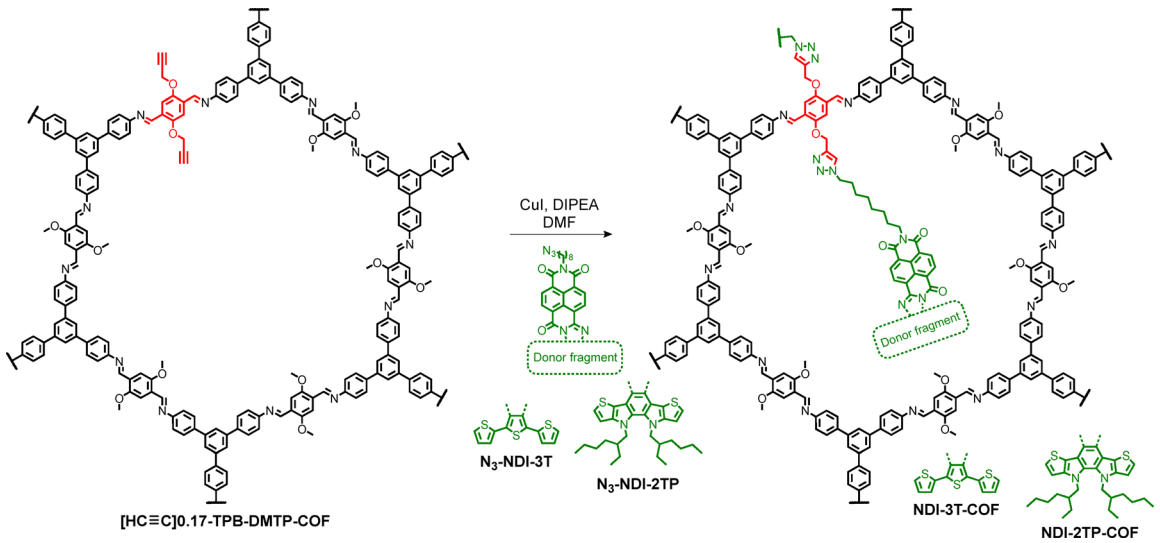

Scheme 2 Synthesis of **NDI-3T-COF** and **NDI-2TP-COF**.

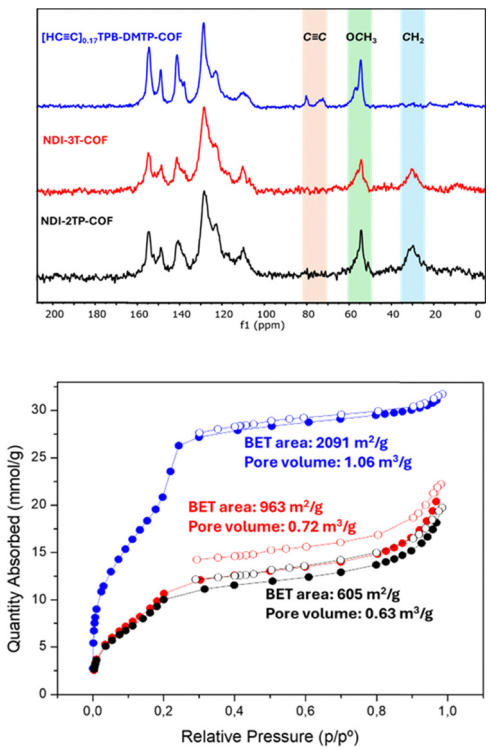

Fig. 1 (Top) Solid-state ^{13}C-CP/MAS-NMR of **[HC≡C]0.17-TPB-DMTP-COF** (blue), **NDI-3T-COF** (red) and **NDI-2TP-COF** (black). Key signal assignments are highlighted. (Bottom) Nitrogen sorption isotherms at 77 K for **[HC≡C]0.17-TPB-DMTP-COF** (blue), **NDI-3T-COF** (red) and **NDI-2TP-COF** (black).

complete loss of the sp-carbon signal in the ^{13}C CP/MAS NMR, confirms that the CuAAC post-synthetic modification proceeded to completion within the sensitivity limits of these analyses.

Nitrogen sorption isotherms measured at 77 K were used to determine the Brunauer–Emmett–Teller (BET) surface areas and pore size distributions of the alkyne-containing precursor and the functionalized COFs, **NDI-3T-COF** and **NDI-2TP-COF** (Fig. 1 and Fig. S19–S21). The mesoporous nature of all three materials was confirmed by the presence of type IV isotherms. As expected, the incorporation of naphthalimide units within the pores resulted in a reduction of both surface area and pore volume parameters (Fig. 1). Thermogravimetric analysis (TGA) demonstrated that **NDI-3T-COF** and **NDI-2TP-COF** exhibit good thermal stability, with decomposition temperatures above 400 °C.

As result of the mild conditions employed in the CuAAC reaction, both **NDI-3T-COF** and **NDI-2TP-COF** retained their crystalline structure, as evidenced by the powder X-ray diffraction (PXRD) patterns shown in Fig. 2 and Fig. S23–S25. However, a set of DFT-based calculations performed using Gaussian 16 C.01[19] and QUANTUM ESPRESSO[20] revealed an unexpected change in the stacking mode of one of the materials. For **NDI-3T-COF**, the eclipsed AA stacking of the parent **[HC≡C]0.17-TPB-DMTP-COF** was preserved, as indicated by the characteristic diffraction peaks at 2.89°, 4.92°, 5.70°, 7.51° and 9.83°, corresponding to the (100), (110), (200), (210) and (220) reflections typical of imine-based COFs (Fig. 2).[21] In contrast, the incorporation of the bulky **NDI-2TP** fragment into the pores of **[HC≡C]0.17-TPB-DMTP-COF** disrupts the eclipsed stacking, resulting in a lateral displacement of the COF layers. Despite this shift, **NDI-2TP-COF** maintains an ordered macromolecular structure, as evidenced by the PXRD data (Fig. 2 and Fig. S23). This change in stacking can be attributed to the presence of 2-ethylhexyl chains in the **NDI-2TP** moiety, which, due to their steric bulk, must be accommodated outside the COF plane—an arrangement only achievable through interlayer displacement. Simulations of **NDI-2TP-COF** with enforced AA stacking produced significantly larger interlayer distances and a PXRD pattern inconsistent with the experimental data thereby conclusively ruling out the eclipsed stacking model. To quantitatively support the structural assignment, Pawley refinements were performed for both COFs, yielding unit cell parameters and *R*-factors in good agreement

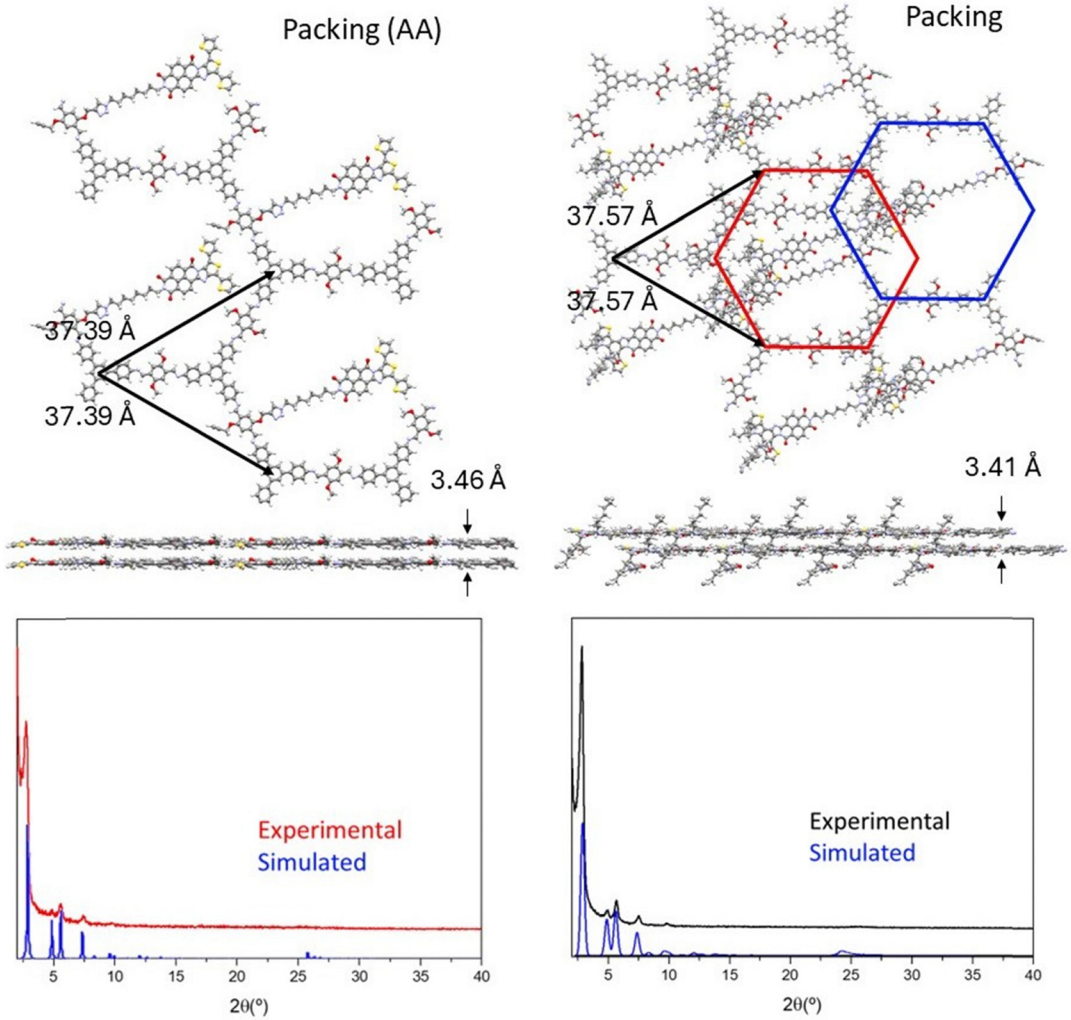

Fig. 2 (Top) Top and side pictorial views of the structures and (down) experimental and simulated diffractograms of **NDI-3T-COF** (left) and **NDI-2TP-COF** (right). The preferential interlaminar distance is indicated. (Bottom) Experimental and simulated diffraction patterns of **NDI-3T-COF** (left) and **NDI-2TP-COF** (right). The simulated pattern of **NDI-3T-COF** corresponds to a unit cell with parameters: $a = b = 37.4$ Å, $c = 3.7$ Å; $\alpha = \beta = 90°$, $\gamma = 120°$. Refinement performed using the Pawley method yielded $R_{wp} = 12.12\%$ and $R_p = 8.86\%$. The simulated pattern of **NDI-2TP-COF** corresponds to a unit cell with parameters: $a = b = 37.6$ Å, $c = 13.6$ Å; $\alpha = \beta = 90°$, $\gamma = 120°$. Refinement performed using the Pawley method yielded $R_{wp} = 12.60\%$ and $R_p = 9.04\%$.

with the experimental data (Fig. S24 and S25). These results confirm the preservation of crystallinity and validate the proposed stacking models for **NDI-3T-COF** and **NDI-2TP-COF**.

Additional morphological characterization by SEM and TEM (Fig. S26–S29) confirmed that both **NDI-3T-COF** and **NDI-2TP-COF** retain their characteristic morphology after post-synthetic modification.

Electrochemical characterization of ORR electrocatalysts

The electrochemical behavior of new synthesized COFs was evaluated both in the absence and in the presence of O_2 in alkaline medium (0.1 M KOH), in order to assess their potential as ORR electrocatalysts. Initially, cyclic voltammetry (CV) measurements under static conditions were performed. In the absence of O_2 (Fig. 3(A)), both COF materials exhibited two redox couples, which are attributed to reversible redox processes involving the enolization of the diimide carbonyl groups.[22–24] For **NDI-2TP-COF**, the redox couples appear at $E1_{red}$ processes associated with the reversible enolation of the diimide carbonyl groups, the slight differences in redox potentials can be attributed to the distinct donor moieties of the newly synthesized COFs, cyclic voltammetry was performed under O_2-saturated conditions (Fig. 3(B)). All COFs materials exhibited higher electrocatalytic activity compared to the Carbon SuperP/GC electrode alone ($E_{onset} = -0.32$ V *vs.* SCE), as evidenced by more positive onset potential and increased current densities during the ORR electrocatalytic process. The most positive onset potential was observed for the **NDI-3T-COF**/Carbon SuperP/GC electrode ($E_{onset} = -0.21$ V *vs.* SCE) followed by the **2TP-COF**/Carbon SuperP/GC electrode ($E_{onset} = -0.23$ V *vs.* SCE). The pristine COF backbone (**[HC≡C]0.17-TPB-DMTP-COF Carbon SuperP/GC**) exhibited an onset potential of $E_{onset} = -0.27$ V *vs.* SCE, supporting the notion that the COF framework contributes to ORR enhancement. However, the superior

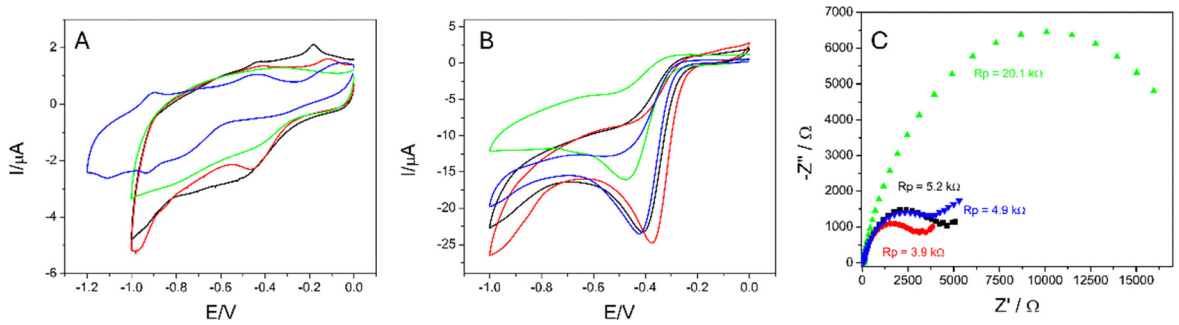

Fig. 3 Cyclic voltammograms of bare Carbon SuperP/GC (green) and modification with **NDI-2TP-COF** (black), **NDI-3T-COF** (red), and **[HC≡C]0.17-TPB-DMTP-COF** (blue) in a 0.1 M NaOH solution (A) in the absence and (B) in the presence of saturated O_2 at 10 mV s^{-1}. (C) Nyquist plot obtained from EIS experiments using bare Carbon SuperP/GC (green) and modification with **NDI-2TP-COF** (black), **NDI-3T-COF** (red), and **[HC≡C]0.17-TPB-DMTP-COF** (blue) in an O_2 saturated 0.1 M NaOH solution (E_{app} = −0.5 V *vs.* SCE).

performance of the NDI-functionalized COFs suggests that the redox-active NDI moieties play a key role in improving electrocatalytic activity. The highest current intensity was also achieved with the **NDI-3T-COF**/Carbon SuperP/GC electrode, further confirming its superior electrocatalytic performance under static electrochemical conditions. To conclude the static electrochemical characterization, electrochemical impedance spectroscopy (EIS) was performed using GC-modified electrodes in O_2-saturated 0.1 M KOH, and the corresponding Nyquist plots were obtained (Fig. 3(C)). This technique enables evaluation of electron transfer resistance during the ORR process for each modified electrode. As anticipated from the cyclic voltammetry results, the **NDI-3T-COF**/Carbon SuperP/GC electrode exhibited the lowest charge transfer resistance (R_p = 3.9 kΩ), indicating the most efficient electron transfer. The **NDI-2TP-COF**/Carbon SuperP/GC and **[HC≡C]0.17-TPB-DMTP-COF** Carbon SuperP/GC showed comparable values (R_p = 5.2 kΩ and R_p = 4.9 kΩ respectively). All COF-based electrodes displayed significantly lower charge transfer resistance than the Carbon SuperP/GC reference (R_p = 20.1 kΩ), confirming the benefit of COF structures in enhancing electron transfer during ORR and supporting their potential as efficient metal-free electrocatalysts.

In addition to impedance measurements, the turnover frequency (TOF) was estimated for both NDI-functionalized COFs to further evaluate their intrinsic catalytic activity. The calculated TOF values were 0.1148 s^{-1} for **NDI-2TP-COF** and 0.1017 s^{-1} for **NDI-3T-COF**, confirming the superior performance of the former. These values are among the highest reported for metal-free COF-based ORR catalysts, underscoring the effectiveness of the donor–acceptor design strategy in enabling rapid catalytic turnover at the molecular level.

The electrocatalytic activity toward the oxygen reduction reaction was further investigated through hydrodynamic electrochemical experiments. Linear sweep voltammograms (LSVs) were recorded using modified rotating ring-disk electrodes (RRDEs) (Fig. 4(A)). The best performance was observed for the **NDI-3T-COF**/Carbon SuperP/GC and **NDI-2TP-COF**/Carbon SuperP/GC electrodes, both exhibiting an onset potential of −0.26 V *vs.* SCE and reaching a current limit of −3.04 mA cm^{-2} at −0.60 V *vs.* SCE. These results clearly outperform those obtained with the Carbon SuperP/GC electrode alone. In this case kinetics limitation during the ORR generates low current broad peaks at high reduction potentials because of different redox process overlaps, such as ORR and hydrogen peroxide reduction. Moderate performance was observed for the COF backbone without electroactive groups (**[HC≡C]0.17-TPB-DMTP-COF**/Carbon SuperP/GC).

The platinum ring currents obtained at 0.25 V *vs.* SCE (Fig. 4(A) dashed lines) were used to calculate the number of electrons transferred during the ORR (Fig. 4(B)). A higher electron transfer number was observed for the **NDI-2TP-COF**/

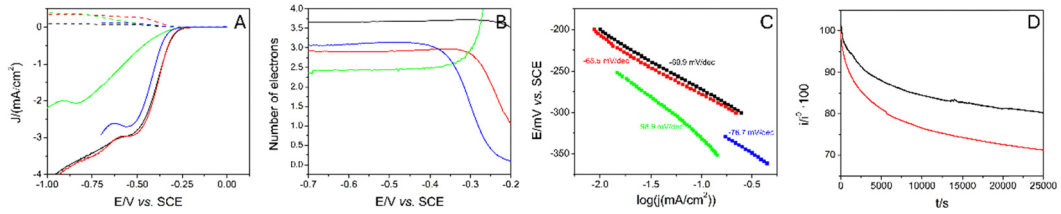

Fig. 4 (A) Hydrodynamic linear sweep voltammetry and (B) number of electrons exchanged in the ORR at different potentials using RRDE of GC/Pt (disc/ring) modified with bare Carbon SuperP/GC (green) and modification with **NDI-2TP-COF** (black), **NDI-3T-COF** (red), and **[HC≡C]0.17-TPB-DMTP-COF** (blue) in an O_2 saturated 0.1 M NaOH solution at 10 mV s^{-1} and 1000 rpm. (C) Tafel slope of ORR electrocatalysis obtained from results in panel A. (D) Current intensity stability of RRDE of GC/Pt electrodes modified **NDI-2TP-COF**/Carbon SuperP (black), and **NDI-3T-COF**/Carbon SuperP (red) electrodes operating in O_2 saturated 0.1 M NaOH solution at a constant potential (−0.5 V *vs.* SCE).

Carbon SuperP/GC electrode, reaching 3.7 electrons—close to the ideal 4-electron pathway desired for fuel cell applications. This result highlights the promising potential of this material as a cathodic electrocatalyst in energy devices.

In contrast, the **NDI-3T-COF**/Carbon SuperP/GC electrode exhibited an average electron transfer number of 2.9, improving over the Carbon SuperP/GC baseline (2.4 electrons), yet still indicating a mixed 2- and 4- electron ORR mechanism. While this represents performance enhancement, it falls short of selectivity toward a single desirable pathway. Consequently, this material is not optimal either for selective hydrogen peroxide production (*via* 2-electron ORR) or for maximum energy output in fuel cell cathodes (*via* 4-electron ORR).

At this point, it is important to highlight the contribution of the electrode used as a support Carbon SuperP/GC during the electrocatalytic ORR process. Carbon SuperP/GC is fundamental during the electrocatalytic process, as it allows the electrocatalysts (**NDI-3T-COF** and **NDI-2TP-COF**) to possess sufficient conductivity to carry out the electrochemical reaction. As we have demonstrated, the ORR process using Carbon SuperP/GC presents slow kinetic, and the ORR mechanism is a mixture of the two possible pathways 2 and 4 electrons, resulting in an average of 2.4 electrons. Furthermore, the limiting current barely exceeds 1 mA cm^{-2} at −0.5 V. Therefore, the contribution of the **NDI-3T-COF** and **NDI-2TP-COF** materials is significant, both in terms of the number of electrons, approaching the ORR *via* the 4-electron mechanism in both cases, and in terms of the limiting current, which is greater than 3 mA cm^{-2} at −0.5 V.

A similar electron transfer number (3.1) was obtained using the pristine COF backbone, **[HC≡C]0.17-TPB-DMTP-COF**/Carbon SuperP/GC, further supporting the presence of a non-selective combination of 2- and 4- electron pathways in the absence of redox-active functionalization.

Tafel slopes (Fig. 4(C)) were derived from the hydrodynamic linear sweep voltammograms shown in Fig. 4(A). The **NDI-2TP-COF**/Carbon SuperP/GC and **NDI-3T-COF**/Carbon SuperP/GC electrodes exhibited Tafel slopes of 69.9 and 69.5 mV dec^{-1}, respectively. These values represent a clear improvement over those obtained with the Carbon SuperP/GC electrode (98.9 mV dec^{-1}) and the pristine COF backbone (**[HC≡C]0.17-TPB-DMTP-COF**/Carbon SuperP/GC (76.7 mV dec^{-1})). These results confirm the enhanced electrocatalytic performance of the NDI-functionalized COFs.

Notably, the Tafel slopes of **NDI-2TP-COF**/Carbon SuperP/GC and **NDI-3T-COF**/Carbon SuperP/GC are very close to that of a **10% Pt-C/SuperP/GC** electrode (68.5 mV dec^{-1}), obtained in other reported works by our group.[23] This is a remarkable result, highlighting that the developed COF-based materials function as highly active, entirely metal-free electrocatalysts for the oxygen reduction reaction.

The stability of the newly developed electroactive COFs materials as ORR electrocatalysts was evaluated by applying a constant potential of −0.5 V *vs.* SCE for 25 ks under hydrodynamic conditions in O_2-saturated 0.1 M NaOH. For the **NDI-3T-COF**/Carbon SuperP/GC electrode, an initial current drop of 20% was observed within the first 2500 s, after which the current stabilized at approximately 75% of its initial value for the remainder of the experiment. In contrast, the **NDI-2TP-COF**/Carbon SuperP/GC electrode showed a smaller initial decrease of 10% over the first 5 ks, maintaining around 87% of the initial current throughout the remaining test period. This represents an excellent stability profile.

These results are particularly noteworthy given the organic nature of the materials and the fact that they are metal-free and non-pyrolyzed, highlighting their robustness as ORR electrocatalysts under continuous operation.

Table 1 contains the main electrochemical results of all the electrodes studied in this work.

Computed O_2 reduction reaction (ORR) mechanisms

To provide a theoretical basis for the experimentally observed differences in oxygen reduction reaction (ORR) performance between **NDI-2TP-COF** and **NDI-3T-COF**, we performed a comprehensive series of density functional theory (DFT) calculations, complemented by Gibbs free energy analyses. These calculations were aimed at evaluating the thermodynamic viability of both the $4e^-$ ORR pathway:

$$\left.\begin{array}{c} O_2 + * + (H^+ + e^-) \rightarrow OOH^* \\ OOH^* + (H^+ + e^-) \rightarrow H_2O + O^* \\ O^* + (H^+ + e^-) \rightarrow OH^* \\ OH^* + (H^+ + e^-) \rightarrow H_2O^* \end{array}\right\}$$
$$\Rightarrow O_2 + (4H^+ + 4e^-) \rightarrow 2H_2O (1.23\,V\ vs.\ SHE) \quad (1)$$

and the $2e^-$ ORR pathway:

$$\left.\begin{array}{c} O_2 + * + (H^+ + e^-) \rightarrow OOH^* \\ OOH^* + (H^+ + e^-) \rightarrow H_2O_2 + * \end{array}\right\}$$
$$\Rightarrow O_2 + (2H^+ + 2e^-) \rightarrow H_2O_2 (0.7\,V\ vs.\ SHE) \quad (2)$$

at the molecular level across various active sites within each COF framework.

Table 1 Summary of the main electrochemical parameters for ORR of 2TP-COF/Carbon SuperP/GC, NDI-3T-COF/Carbon SuperP/GC, ([HC≡C]$_{0.17}$-TPB-DMTP-COF/Carbon SuperP/GC and Carbon SuperP/GC)

Electrode	E_{onset} *vs.* SCE/mV	j_{lim}/(mA cm^{-2})	Tafel slope/(mV dec^{-1})	R_p/kΩ	ORR number of electrons	$\eta_{experimental}$/mV
2TP-COF/Carbon SuperP/GC	−264	−2.97	−69.9	5.2	3.7	484
NDI-3T-COF/Carbon SuperP/GC	−265	−2.95	−68.5	3.9	2.9	485
[HC≡C]0.17-TPB-DMTP-COF/Carbon SuperP/GC	−307	−2.70	−76.7	4.9	3.1	527
Carbon SuperP/GC	−330	−2.08	−98.9	20.1	2.4	550

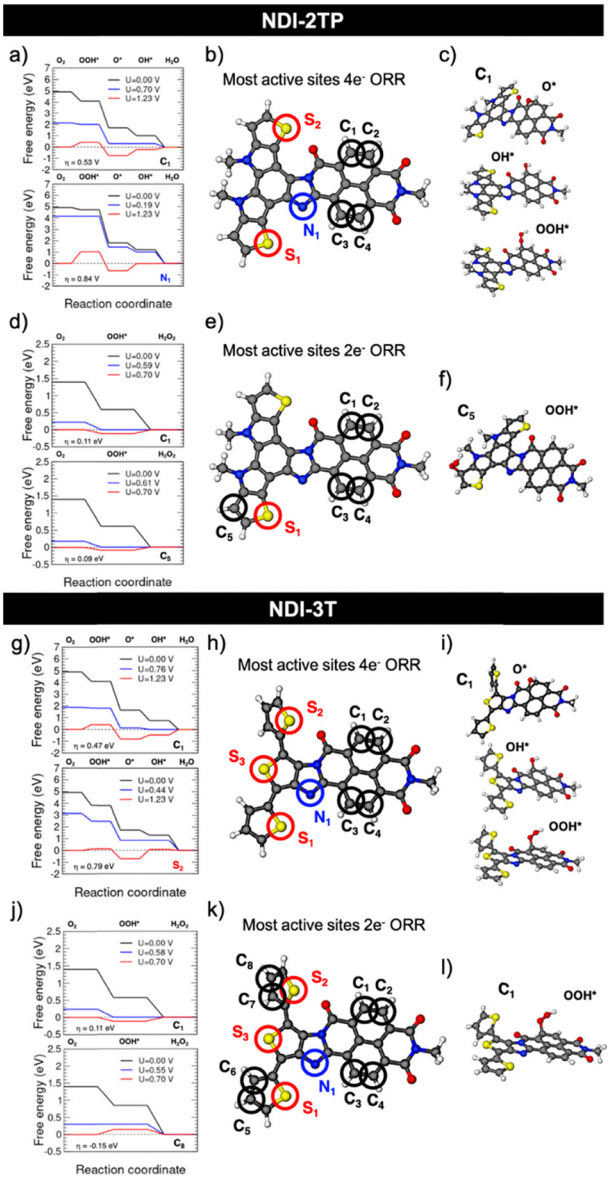

Fig. 5 (a) and (d) Free energy change along the 4e⁻ ORR (a) and 2e⁻ ORR (d) pathways computed at 298.15 K and pH = 0 in water for the two most active sites at three different electrode potentials *vs.* SHE: U = 0 V (black line), working potential (blue line) and equilibrium potential (red line) for the **NDI-2TP** fragment. (b) and (e) Most active 4e⁻ ORR (a) and 2e⁻ ORR (b) sites theoretically predicted for the **NDI-2TP** fragment. (c) DFT-optimized structure for the 4e⁻ ORR (c) and 2e⁻ ORR (f) intermediates for the most active site in the **NDI-2TP** fragment. (g)–(l) Same information of panels (a)–(f) for the **NDI-3T** system.

For the **NDI-2TP** system, theoretical modeling reveals seven distinct 4e⁻ ORR active sites exhibiting overpotentials $|\eta| <$ 1.2 V (C_1–C_4, N_1, S_1 and S_2) able to catalyze the complete reduction of O_2 to H_2O, with overpotentials ranging from 0.53 to 1.07 V (see Fig. 5a and b). Fig. 5c shows the DFT-optimized structure for the 4e⁻ ORR intermediates for the most active site (C_1). In all cases except for N_1, the rate-limiting step (establishing the $\eta_{4e\text{-ORR}}$ overpotential value) is the proton-coupled electron transfer from adsorbed atomic oxygen to adsorbed OH*, O* + $(H^+ + e^-)$ → OH*, which is typically associated with strong oxygen adsorption that hinders O desorption. For the N_1 site the limiting step shifts to the initial activation of O_2, $O_2 + * + (H^+ + e^-)$ → OOH*, indicating a weaker initial O_2 binding affinity at that site. Despite the moderately high overpotentials observed in some sites, all values lie within the range considered viable for practical electrocatalysis. In addition, theoretical analysis predicts six sites yielding $|\eta| <$ 0.5 V (most of them coincident with the 4e⁻ ORR active sites) exhibiting activity toward the 2e⁻ ORR pathway, with significantly lower overpotentials: 0.09–0.39 V for the C_1–C_5 and S_1 sites (see Fig. 5d and e). In all cases the rate-limiting step (establishing the $\eta_{2e\text{-ORR}}$ overpotential value) is the final proton-coupled electron transfer OOH* + $(H^+ + e^-)$ → H_2O_2 sub-reaction. Fig. 5f shows the DFT-optimized structure for the 2e⁻ ORR intermediate for the most active site (C_5). However, a key mechanistic insight is that most of the active sites show exceptionally strong O* binding, with ΔG_{O^*} values all below 2 eV, compared to the ideal value of 2.46 eV for the ideal/balanced 4e⁻ ORR catalyst. This strong binding energetically favors O–O bond cleavage from the OOH* intermediate, steering the reaction toward full O_2 reduction to H_2O even when the 2e⁻ route is thermodynamically accessible. From a kinetic standpoint, the reaction barriers for OOH* dissociation (leading to O* and eventually to OH*) are expected to be lower due to the stabilization of intermediates by the electronic structure of the COF framework. This accelerates the 4e⁻ pathway relative to the 2e⁻ route, where OOH* desorption would otherwise dominate. Consequently, despite the favourable thermodynamics of the 2e⁻ route at some sites, the kinetics clearly favour almost complete O–O bond scission and full reduction, leading to the experimentally observed average electron transfer number of 3.7, remarkably close to the ideal 4e⁻ ORR process. Such a high degree of selectivity is rare for metal-free COFs, underscoring **NDI-2TP-COF** as a high-performance ORR catalyst for fuel cell cathodes, where selective and almost complete reduction to H_2O is essential to avoid H_2O_2 accumulation.

In contrast, **NDI-3T** system displays a more heterogeneous electrocatalytic behaviour. Eight 4e⁻ ORR active sites similarly exhibiting $|\eta| <$ 1.2 V were theoretically identified (C_1–C_4, N_1, S_1–S_3) with overpotentials ranging from 0.47 to 1.13 V (see Fig. 5g and h). Fig. 5i shows the DFT-optimized structure for the 4e⁻ ORR intermediates for the most active site (C_1). However, the distribution of these sites includes several with relatively high kinetic barriers, which could bottleneck the overall catalytic performance in the 4e⁻ pathway. Again, in all cases except for C_1, the rate-limiting step (establishing the $\eta_{4e\text{-ORR}}$ overpotential value) is O* + $(H^+ + e^-)$ → OH*. For the C_1 site the limiting step shifts to the final OH* + $(H^+ + e^-)$ → H_2O sub-reaction.

Moreover, remarkably, a large amount of twelve 2e⁻ ORR active sites (double than for the **NDI-2TP** case) yielding $|\eta| <$ 0.5 V exhibit favorable 2e⁻ ORR activity (C_1–C_8, N_1, S_1–S_3) with overpotentials ranging from −0.15 to 0.47 V (see Fig. 5j and k). Fig. 5l shows the DFT-optimized structure for the 2e⁻ ORR

intermediate for the most active site (C_5). While low ΔG_{O^*} values are also observed in this system, as in **NDI-2TP-COF**, the stronger thermodynamic driving force for the $2e^-$ pathway at a larger number of sites suggests a broader mechanistic competition between O–O bond cleavage and retention. In all cases except for C_8, the rate-limiting step (establishing the $\eta_{2e\text{-}ORR}$ overpotential value) is the final proton-coupled electron transfer $OOH^* + (H^+ + e^-) \rightarrow H_2O_2$ sub-reaction. For the C_8 site the limiting step is the initial activation of O_2, $O_2 + * + (H^+ + e^-) \rightarrow OOH^*$. This dual-pathway behavior is confirmed experimentally by an average electron transfer number of 2.9, reflecting a non-selective mixture of the $2e^-$ and $4e^-$ ORR mechanisms. Although this represents a significant improvement over the baseline SuperP/GC system (2.4 electrons), it falls short of ideal behavior for either complete water production or selective H_2O_2 synthesis. The kinetic scenario here likely involves competition between OOH* dissociation and desorption, with site-to-site variability preventing a dominant pathway from emerging, ultimately reducing overall selectivity.

Further comparison with **[HC≡C]0.17-TPB-DMTP-COF**, a structurally distinct material with an intermediate value of 3.1 electrons, reinforces the importance of structural and electronic design in governing ORR selectivity. Specifically, the extended conjugation, electron-deficient NDI core, and strategic placement of heteroatoms in **NDI-2TP-COF** collectively enable stronger O* stabilization and lower kinetic barriers for O–O bond cleavage, thereby favoring the $4e^-$ mechanism. In contrast, the more delocalized and less directional reactivity of **NDI-3T-COF** leads to non-selective behavior.

In conclusion, DFT and Gibbs free energy analyses provide robust mechanistic evidence supporting the nearly exclusive $4e^-$ ORR selectivity in **NDI-2TP-COF**. The confluence of strong O* binding, favorable kinetics for O–O cleavage, and moderate overpotentials establishes a highly active and selective catalytic environment for full O_2 reduction. In contrast, **NDI-3T-COF** lacks this mechanistic coherence, resulting in reduced selectivity and efficiency. These findings highlight the power of rational COF design in tuning both thermodynamic and kinetic parameters for targeted electrochemical applications in sustainable energy conversion.

Conclusions

In this study, we successfully developed two novel metal-free electrocatalysts, **NDI-3T-COF** and **NDI-2TP-COF**, *via* post-synthetic functionalization of a covalent organic framework with donor–acceptor (D–A) motifs. Structural and spectroscopic analyses confirmed the effective integration of active sites into the COF backbone, while preserving crystallinity and porosity. Electrochemical measurements revealed that both materials exhibit enhanced oxygen reduction reaction (ORR) activity compared to the pristine COF and carbon-based benchmarks, with **NDI-2TP-COF** displaying superior onset potential, electron transfer number, and long-term stability. Density functional theory (DFT) calculations provided mechanistic insights, showing that the electronic structure of **NDI-2TP-COF** promotes a 4-electron ORR pathway with low overpotentials and efficient O–O bond cleavage. These results highlight the potential of rational D–A design in COFs for the development of high-performance, metal-free electrocatalysts for sustainable energy conversion technologies.

Author contributions

E. G.: investigation, data curation, visualization, writing – original draft, writing – review and editing. E. M.-P.: investigation, data curation, visualization, writing – original draft, writing – review and editing, funding acquisition, project administration. M. M.-F. data curation, writing – original draft, writing – review and editing. J. I. M.: conceptualization, investigation, data curation, visualization, writing – original draft, writing – review and editing. M. G.-L.: investigation, data curation, writing – review and editing. J. L. S.: conceptualization, investigation, visualization, supervision, writing – review and editing, funding acquisition, project administration.

Conflicts of interest

There are no conflicts to declare.

Data availability

The experimental and theoretical data supporting this article have been included as part of the supplementary information (SI). Supplementary information is available. See DOI: **https://doi.org/10.1039/d5qm00655d**.

Acknowledgements

This work was financially supported by MICINN (PID2022-138908NB-C33, TED2021-129886BC43 and PID2022-142262OA-I00) and the UCM (INV.GR.00.1819.10759). J. L. S. acknowledge the MICINN for the REDES project "RED2022-134503-T" and the Comunidad de Madrid (TEC-2024/ECO-332).

References

1 M. Martínez-Fernández and J. L. Segura, Exploring Advanced Oxygen Reduction Reaction Electrocatalysts: The Potential of Metal-Free and Non-Pyrolyzed Covalent Organic Frameworks, *ChemSusChem*, 2024, **17**, e202400558.
2 R. Ma, G. Lin, Y. Zhou, Q. Liu, T. Zhang, G. Shan, M. Yang and J. Wang, A review of oxygen reduction mechanisms for metal-free carbon-based electrocatalysts, *npj Comput. Mater.*, 2019, **5**, 78.
3 M. Shao, Q. Chang, J. P. Dodelet and R. Chenitz, Recent Advances in Electrocatalysts for Oxygen Reduction Reaction, *Chem. Rev.*, 2016, **116**, 3594–3657.
4 T. Xu, H. Zhou, X. Zhang, T. S. Herng, J. Ding, C. Chi and J. Zhu, Covalent Organic Frameworks with Carbon-Centered

Radical Sites for Promoting the 4e− Oxygen Reduction Reaction, *Angew. Chem., Int. Ed.*, 2025, **64**, e202424449.
5 D. Grumelli, B. Wurster, S. Stepanow and K. Kern, Bio-inspired nanocatalysts for the oxygen reduction reaction, *Nat. Commun.*, 2013, **4**, 2904.
6 M. K. Debe, Electrocatalyst approaches and challenges for automotive fuel cells, *Nature*, 2012, **486**, 43–51.
7 Y. Yang, Y. Lu, H. Y. Zhang, Y. Wang, H. L. Tang, X. J. Sun, G. Zhang and F. M. Zhang, Decoration of Active Sites in Covalent-Organic Framework: An Effective Strategy of Building Efficient Photocatalysis for CO2 Reduction, *ACS Sustainable Chem. Eng.*, 2021, **9**, 13376–13384.
8 Q. Xu, Y. Tang, X. Zhang, Y. Oshima, Q. Chen and D. Jiang, Template Conversion of Covalent Organic Frameworks into 2D Conducting Nanocarbons for Catalyzing Oxygen Reduction Reaction, *Adv. Mater.*, 2018, **30**, 1706330.
9 X. Yan, B. Wang, J. Ren, X. Long and D. Yang, An Unsaturated Bond Strategy to Regulate Active Centers of Metal-Free Covalent Organic Frameworks for Efficient Oxygen Reduction, *Angew. Chem., Int. Ed.*, 2022, **61**, e202209583.
10 P. Bai and L. Xu, Toward a unified pH-performance picture of active sites in nitrogen-doped carbon materials, *Appl. Catal., B*, 2025, **365**, 124908.
11 J. Barrio, J. Li and M. Shalom, Carbon Nitrides from Supramolecular Crystals: From Single Atoms to Heterojunctions and Advanced Photoelectrodes, *Chem. – Eur. J.*, 2023, **29**, e202302377.
12 R. Bao, Z. Xiang, Z. Qiao, Y. Yang, Y. Zhang, D. Cao and S. Wang, Designing Thiophene-Enriched Fully Conjugated 3D Covalent Organic Framework as Metal-Free Oxygen Reduction Catalyst for Hydrogen Fuel Cells, *Angew. Chem., Int. Ed.*, 2023, **62**, e202216751.
13 M. Martínez-Fernández, E. Martínez-Periñán, J. I. Martínez, M. Gordo-Lozano, F. Zamora, J. L. Segura and E. Lorenzo, Evaluation of the Oxygen Reduction Reaction Electrocatalytic Activity of Postsynthetically Modified Covalent Organic Frameworks, *ACS Sustainable Chem. Eng.*, 2023, **11**, 1763–1773.
14 S. Huang, S. Lu, Y. Hu, Y. Cao, Y. Li, F. Duan, H. Zhu, Y. Jin, M. Du and W. Zhang, Covalent Organic Frameworks with Molecular Electronic Modulation as Metal-Free Electrocatalysts for Efficient Hydrogen Peroxide Production, *Small Struct.*, 2023, **4**, 2200387.
15 G. Kumar, S. K. Das, T. R. K. Rana, S. Samui, L. Billon and R. S. Dey, Donor–acceptor covalent organic frameworks propel the oxygen reduction reaction with push–pull dynamics, *J. Mater. Chem. A*, 2024, **12**, 28085–28094.
16 F. Suárez-Blas, L. Pandolfi, M. J. Alonso-Navarro, S. Riera-Galindo, J. I. Martínez, B. Dörling, A. Funes, A. Harillo-Baños, E. Venuti, M. M. Ramos, M. Campoy-Quiles and J. L. Segura, Tailoring the Electron-Deficient Central Core on Fused-Ring Nonfullerene Acceptors: Deciphering the Relationships Between Structure, Property, and Photovoltaic Performance, *Adv. Energy Sustainable Res.*, 2024, **5**, 2400028.
17 R. González-Núñez, M. J. Alonso-Navarro, F. Suárez-Blas, E. Gala, M. M. Ramos, J. L. Segura and R. Ponce Ortiz, Tuning the charge stabilization and transport in naphthalimide-based semiconductors via a fused-ring and core-engineering strategy, *Mater. Chem. Front.*, 2024, **8**, 1981–1992.
18 K. Tambara, N. Ponnuswamy, G. Hennrich and G. D. Pantoş, Microwave-assisted synthesis of naphthalenemonoimides and N-desymmetrized naphthalenediimides, *J. Org. Chem.*, 2011, **76**, 3338–3347.
19 M. J. Frisch, G. W. Trucks, H. B. Schlegel, G. E. Scuseria, M. A. Robb, J. R. Cheeseman, G. Scalmani, V. Barone, G. A. Petersson, H. Nakatsuji, X. Li, M. Caricato, A. V. Marenich, J. Bloino, B. G. Janesko, R. Gomperts, B. Mennucci, H. P. Hratchian, J. V. Ortiz, A. F. Izmaylov, J. L. Sonnenberg, D. Williams, F. Ding, F. Lipparini, F. Egidi, J. Goings, B. Peng, A. Petrone, T. Henderson, D. Ranasinghe, V. G. Zakrzewski, J. Gao, N. Rega, G. Zheng, W. Liang, M. Hada, M. Ehara, K. Toyota, R. Fukuda, J. Hasegawa, M. Ishida, T. Nakajima, Y. Honda, O. Kitao, H. Nakai, T. Vreven, K. Throssell, J. A. Jr., J. E. Peralta, F. Ogliaro, M. J. Bearpark, J. J. Heyd, E. N. Brothers, K. N. Kudin, V. N. Staroverov, T. A. Keith, R. Kobayashi, J. Normand, K. Raghavachari, A. P. Rendell, J. C. Burant, S. S. Iyengar, J. Tomasi, M. Cossi, J. M. Millam, M. Klene, C. Adamo, R. Cammi, J. W. Ochterski, R. L. Martin, K. Morokuma, O. Farkas, J. B. Foresman and D. J. Fox, *Gaussian 16, Revision C.01*, 2016.
20 P. Giannozzi, S. Baroni, N. Bonini, M. Calandra, R. Car, C. Cavazzoni, D. Ceresoli, G. L. Chiarotti, M. Cococcioni, I. Dabo, A. Dal Corso, S. de Gironcoli, S. Fabris, G. Fratesi, R. Gebauer, U. Gerstmann, C. Gougoussis, A. Kokalj, M. Lazzeri, L. Martin-Samos, N. Marzari, F. Mauri, R. Mazzarello, S. Paolini, A. Pasquarello, L. Paulatto, C. Sbraccia, S. Scandolo, G. Sclauzero, A. P. Seitsonen, A. Smogunov, P. Umari and R. M. Wentzcovitch, QUANTUM ESPRESSO: a modular and open-source software project for quantum simulations of materials, *J. Phys.: Condens. Matter*, 2009, **21**, 395502.
21 H. Xu, J. Gao and D. Jiang, Stable, crystalline, porous, covalent organic frameworks as a platform for chiral organocatalysts, *Nat. Chem.*, 2015, **7**, 905–912.
22 X. Wu, Y. Qi, J. J. Hong, Z. Li, A. S. Hernandez and X. Ji, Rocking-Chair Ammonium-Ion Battery: A Highly Reversible Aqueous Energy Storage System, *Angew. Chem., Int. Ed.*, 2017, **56**, 13026–13030.
23 M. Martínez-Fernández, E. Martínez-Periñán, J. I. Martínez, M. Gordo-Lozano, F. Zamora, J. L. Segura and E. Lorenzo, Evaluation of the Oxygen Reduction Reaction Electrocatalytic Activity of Postsynthetically Modified Covalent Organic Frameworks, *ACS Sustainable Chem. Eng.*, 2023, **11**, 1763–1773.
24 H. H. Tsai, T. J. Lin, B. Vedhanarayanan, C. C. Tsai, T. Y. Chen, X. Ji and T. W. Lin, A 1.9-V all-organic battery-supercapacitor hybrid device with high rate capability and wide temperature tolerance in a metal-free water-in-salt electrolyte, *J. Colloid Interface Sci.*, 2022, **612**, 76–87.